3D Mapping Database Aided GNSS RTK and Its Assessments in Urban Canyons

Hoi-Fung Ng[1] and Li-Ta Hsu[1]*

1 Interdisciplinary Division of Aeronautical and Aviation Engineering, The Hong Kong Polytechnic University

* lt.hsu@polyu.edu.hk

Abstract— Different revolutionary applications, like the unmanned autonomous systems (UAS), require a highly precise positioning with centimetre-level accuracies. And Real-Time Kinematic (RTK) GNSS positioning stands a chance to these potential applications. RTK positioning can provide a centimetre-level positioning in open-sky or sub-urban environments. However, the performance is limited in a deep urban canyon with severe multipath and cycle slip effects. The measurements with noise will introduce error and results in bad solution quality. Therefore, removal on the bad measurements and remain those good-condition signals become essential for performing RTK in the urban environment. Based on this idea, this paper proposes using 3D building model with position hypothesis to select the healthy satellites for RTK positioning. We believed that using the 3D building model can better exclude the unhealthy or non-line-of-sight (NLOS) satellite compare to using a fixed high elevation angle mask. Therefore, this paper will compare the position results between 3D mapping aided (3DMA) GNSS RTK and the GNSS RTK with a fixed elevation angle mask. Geodetic- and commercial-grade receivers are employed to perform experiments in the urban environment of Hong Kong. The experiment results with geodetic-grade receiver shows that 3DMA GNSS RTK can provide a positioning accuracy with 10cm averagely.

*Index Terms—*GNSS; Navigation; RTK; 3D building model; Urban canyons; Multipath; NLOS; 3DMA GNSS

I. INTRODUCTION

GNSS is widely adopted in different unmanned autonomous system (UAS). With the differential GNSS (DGNSS) correction, smartphones or low-cost receivers can achieve one to two meters positioning error. However, positioning in the urban environment is always a challenge for GNSS positioning, where buildings can block, reflect or diffract the signals. Once the receiver receives these noisy measurements, it will degrade the positioning performance. For positioning with code measurements only in the urban environment, different techniques have been implemented to identify and exclude or correct those unhealthy measurements. They were starting with urban positioning strategies with extra equipment, which is suitable for vehicle-mounted applications. [1, 2] proposed using the sky-pointing fisheye camera to exclude the NLOS satellites by image recognition. Another approach is using a 3D light detection and ranging (LiDAR) to provide surrounding environment obstacles and detect the NLOS signal [3]. LiDAR can estimate the distance between building and itself as well as the visibility of the satellite. Therefore, with the NLOS propagation model, the reflection delay of the NLOS classified satellite can be predicted [4]. By integrating with the sky-pointing fisheye camera with LiDAR, the positioning accuracy in urban areas can be improved [5]. Also, research on the tightly-coupled GNSS/INS system for autonomous navigation in urban areas [6].

Followed by the receiver based urban positioning techniques, consistency-check method [7] can detect and exclude those unhealthy measurements to obtain better positioning accuracy. The trend on 3D building model resources become open access, which can aid the positioning in the urban environment. It is well-known as 3D mapping aided (3DMA) GNSS [8]. Common 3DMA GNSS algorithms are NLOS-excluded positioning [9], shadow matching [10, 11], likelihood-based 3DMA GNSS [12], ray-tracing 3DMA GNSS [13-15], and skymask 3DMA GNSS [16]. The integrated solution of 3DMA GNSS can achieve accuracy within 10-meter in the urban environment in both along and across street accuracy [12].

Although the range-based GNSS can achieve several meters accuracy suitable for smartphone and IoT applications, it is not for UAS, which requires a high precision positioning accuracy. Therefore, a higher resolution measurement, which is carrierphase measurement, is required to provide finer positioning accuracy. Real-time kinematic (RTK) positioning stands a chance for the application which requires centimetre-level accuracy positioning. RTK positioning is one of the most precise positioning technologies currently, which cooperates carrierphase measurements based on relative positions to obtain a centimetre-level accuracy positioning [17]. Conventionally GNSS RTK positioning is used to employ by limited applications operating in open-sky environment such as a geodetic survey. RTK positioning brings the sub-meter-level positioning accuracy to centimetre-level one. In conventional RTK positioning [18], the float position and float ambiguities are obtained by the least square method. Then the ambiguity resolution (AR) is performed by least-squares ambiguity decorrelation (LAMBDA) method to search for the optimal integer set in the ambiguity search ellipsoid. After the AR process, the integer ambiguities with minimum mean squared error (MMSE) can be found. The MMSE integer set becomes the fixed solution, and this method is named integer least squares (ILS) estimation [19]. The ratio test is to examine the confidence of integer set with MMSE to be unlike across other integer sets within searching space [20]. Low likelihood of the fixed integer set means it can be discriminated with enough confidence to provide precise position. The critical value is derived empirically with testing data, a threshold of 3 is usually used as a rule of thumb for ratio test validation [21]. There is also other research using a different critical value for ratio test, like k = 1.5 [22] and k = 2 [23]. Another method to obtains a fixed solution is the best integer equivariant (BIE) estimator [24, 25]. The BIE-estimator is optimal in the MMSE sense by weighted averaging all integer sets in AR processes. The BIE-estimator, therefore, outperforms the float solutions and maintains the same accuracy as the fixed ILS solutions. Furthermore, no integer validation test is required.

Different researches have shown that RTK can provide high accuracy positioning solution in open-sky as well as some sub-urban environments [26]. Other studies also show that multi-constellation and -frequencies can achieve a higher fixing rate [27-30]. However, centimetre-level accuracy positioning with RTK is still a challenge even with measurements from multi-constellation and frequencies. In a highly urbanised environment surrounded by tall buildings, the GNSS signal can be reflected or diffracted, which results in NLOS reception and multipath effects. Where research shows that the multipath effect with lack of multipath suppression technique can results in increment on time to ambiguity resolution (TAR) [31]. Another serious problem, especially for carrierphase measurement, is the cycle slip effect due to the loss of lock for the signals [32]. These uncertainties for carrierphase measurements may result in incorrect ambiguity resolution (AR) processes with a low fixing rate [26]. To achieve better performance of RTK positioning in urban environments, excluding the unhealthy measurements is one of the approaches. A research in [33] proposed a cycle slip detection scheme and fixed by the MEMS-IMU to perform the RTK positioning. In [34], implemented using the sky-pointing fisheye camera with image processing technique to exclude the NLOS received satellites. Where this approach is suitable for vehicle-mounted application such as autonomous driving, another research does not require any extra equipment to improve the performance of RTK in the urban environment, such as selecting satellite with signal-to-noise ratio (SNR) [35] and increase the cut-off elevation angles [36]. These approaches can improve the availability of RTK GNSS in the urban canyon.

At the meanwhile, some of the researches proposed cooperating the 3D building model to aid the RTK positioning. One innovation approach is the continuous-LOS method [37]. It assumes the signals that can be tracked continuously indicating a good quality of the measurements. Therefore, better positioning results can be obtained with only healthy measurements. These researches show that the selection of correct (e.g., LOS) satellites for RTK is important. Also, [38] proved that RTK GNSS could be achieved when approximate positions were within 5-15m from the true position with the aids of 3D maps. For the UAS application, the 3D maps can help the path planning to avoid GNSS challenging places and maximize the performance of RTK GNSS [39].

This paper aims to incorporate RTK positioning with the 3DMA position hypothesis method to select the optimal satellites for AR process, named as 3DMA GNSS RTK. Excluding unhealthy satellites based on the building geometry is the key strength of the proposed method. This strength is obvious for RTK receivers located at the environment with unevenly distributed buildings where the elevation angle mask should variate along with all azimuth angles.

Several designed experiments on both urban and suburban environments in Hong Kong are performed to evaluate positioning performance on with and without 3DMA, as well as with different elevation angle cut-off value.

The remainder of this paper is organised as follows: the system overview of the proposed 3DMA GNSS RTK is introduced in section 2. The experiments result, and analysis is presented in section 3. Finally, section 4 includes the conclusion and future works.

II. THE PROPOSED 3DMA GNSS RTK

The flowchart of the proposed 3DMA GNSS RTK is shown in Fig. 1. The algorithm can be divided into the online and offline processes. The offline stage includes processing the 3D building model for NLOS classification. Here, we utilise the resource from GNSS shadow matching, which is the skyplot with highest elevation angle of the building boundaries, as known as 'skymask'. The process will be discussed in section Fig. 1. At the online stage, the real-time RTK positioning and 3DMA GNSS RTK are performed. First, the conventional RTK positioning with ambiguity resolution is performed and used as an initial guess. Based on the RTK solution, the hypothesis positioning candidates can be distributed. On each candidate, the satellite visibility will be estimated, then find the float solution and followed by ambiguity resolution. The carrierphase measurements with fixed ambiguities will then be used to estimate the weighting of the candidates, and the weighted average candidates' position can be found. This weighted average position is used as an accurate float solution for the 3DMA GNSS RTK. The float solution will then perform NLOS exclusion and ambiguity resolution by BIE-estimator again to find the final solution.
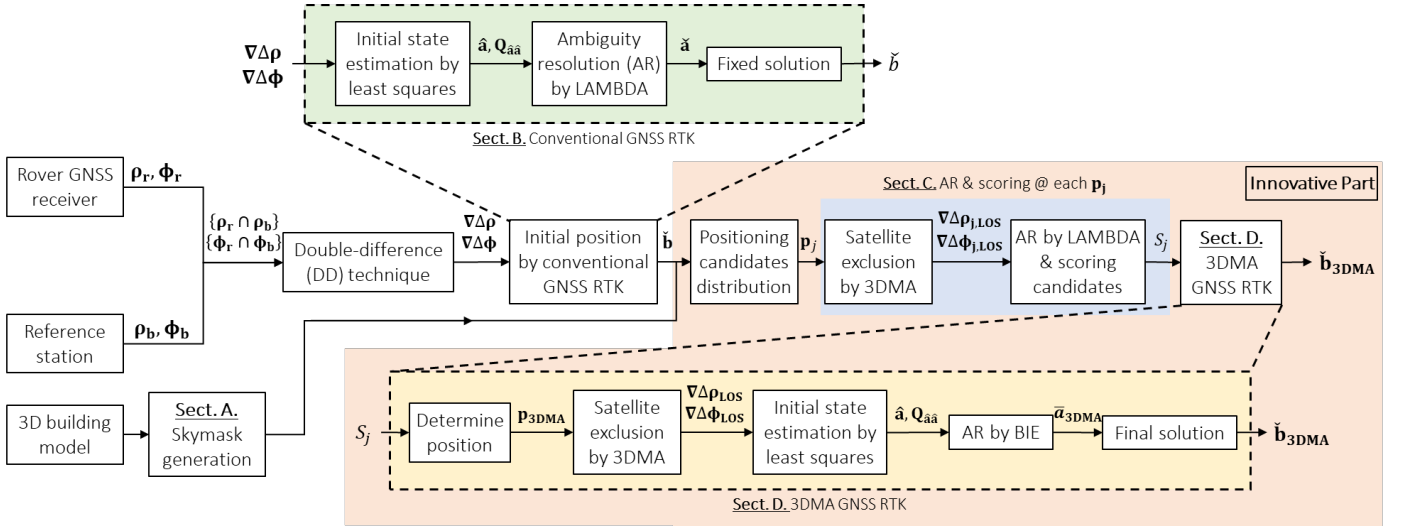
A. Skymask Generation

The resources used in GNSS shadow matching are utilised for LOS/NLOS classification at each candidate, which is the 'skymask'. 'Skymask' is the skyplot with the building boundaries with the highest elevation angle. The skymask generation process is needed for NLOS classification at real-time positioning stage. The skymask generation is done offline to reduce the computation load for the receiver. The detailed skymask generation processes can be found in [16].

A large area of 3D building model is required to increase the availability of this algorithm as well as other 3DMA GNSS algorithms, which can be obtained by combining satellite images and airborne LiDAR [40, 41]. The 3D building model covered area is divided into grid point. At each grid point j, the skymask $el_{skymask,j}(az)$ is generated in 1-degree resolution on azimuth angle az and 0.1-degree resolution on elevation angle. The satellite is placed on the skymask to classify the i-th satellite SV^i to LOS/NLOS. If the satellite elevation angle is higher than that of skymask at a corresponding azimuth angle, it will be classified as LOS, SV_{LOS}. Vice versa, the satellite will be NLOS, SV_{NLOS}.

$$SV_{LOS} = \{SV \in SV^i \mid el^i > el_{skymask,j}(az^i)\}$$
$$SV_{NLOS} = \{SV \in SV^i \mid el^i \leq el_{skymask,j}(az^i)\} \quad (1)$$

The pre-processed skymask are stored in the server-side. When performing real-time positioning, the skymask can be downloaded from the server.

B. Conventional GNSS RTK for Initial Guess

GNSS RTK cooperates both code (pseudorange) and carrierphase measurements to resolve the rover (receiver) position by estimating the relative distance to a reference station. In this paper, we use multi-constellation and dual-frequency measurements. All measurements will perform a simple selection with C/N_0 larger than 15dB-Hz and elevation angle el larger than 15-degrees. The implemented GNSS RTK is based on the [42]. The equations in this Section B are fundamental to the derivation of the proposed hypothesised 3DMA GNSS RTK.

The double-differenced (DD) formulation is in system-specific pivot satellite manner, where one master satellite, $*^m$, for each constellation and measurement frequency. Their DD code $\nabla\Delta\rho$ and carrier $\nabla\Delta\phi$ measurements for the i-th and commonly received satellite at both rover SV_r and base station SV_b can be expressed in meter, as,

$$\nabla\Delta\rho^i = \rho_r^i - \rho_r^m - (\rho_b^i - \rho_b^m) = \nabla\Delta D^i + \varepsilon_{\rho^i}$$
$$\nabla\Delta\phi^i = \phi_r^i - \phi_r^m - (\phi_b^i - \phi_b^m) \quad (2)$$
$$= \nabla\Delta D^i + \lambda^i\nabla\Delta N^i + \varepsilon_{\phi^i}$$

where $*_r$ stands for rover data while $*_b$ stands for base station data. $\nabla\Delta D$ is the double-differenced geometry distance. ε_* is other error terms from receiver noise, etc. λ^i is the wavelength of the i-th common satellite between rover and base station (excluding the master one). $\nabla\Delta N$ is the double differenced integer ambiguity, where this will be obtained by AR which will be discussed in the sub-section 2).

We assume the distance between rover and reference station is short, e.g. smaller than 10km, hence the atmospheric error can be almost eliminated by DD. As well as the satellite and receiver clock error can be eliminated by DD. In other words, the remaining element after DD should be the DD geometric distance $\nabla\Delta D$ between satellite, rover and reference station, and other noise ε. The geometric distance for satellite i to the receiver is calculated by the Pythagoras theorem of satellite ECEF position and receiver ECEF position,

$$D_*^i = \|\mathbf{p}^i - \mathbf{p}_*\|$$
$$= \sqrt{(p_x^i - p_{*,x})^2 + (p_y^i - p_{*,y})^2 + (p_z^i - p_{*,z})^2} \quad (3)$$

Noted that geometric distance is applicable for both rover and reference station, D_r^i and D_b^i, respectively. Therefore, the DD of the geometric distance between receiver and satellite can be expressed as,

$$\nabla\Delta D^i = D_r^i - D_r^m - (D_b^i - D_b^m) \quad (4)$$

This DD geometric distance can be used to form the known term vector for least square estimation. It represents the baseline distance between rover and reference station.

1) Initial Float Value Estimation by Least-Squares

The initial state estimation on the float position and

ambiguities is done by the least-squares method. Where the state and DD observation model can be linearized as follows,
$$\mathbf{y} = \mathbf{Ax} \tag{5}$$
where $\mathbf{y}$ is the measurement vector,
$$\mathbf{y} = \begin{bmatrix} \nabla\Delta\rho^1 - \nabla\Delta D^1 \\ \vdots \\ \nabla\Delta\rho^i - \nabla\Delta D^i \\ \nabla\Delta\phi^1 - \nabla\Delta D^1 \\ \vdots \\ \nabla\Delta\phi^i - \nabla\Delta D^i \end{bmatrix} \tag{6}$$

$\mathbf{A}$ is the design matrix of the baseline and ambiguities. The first three columns of design matrix are the difference of the unit LOS vector for the satellites. While the upper right is a zero matrix and lower right is a diagonal matrix of the wavelength for corresponding satellite.

$$\mathbf{A} = \begin{bmatrix} \mathbf{u_r^1} - \mathbf{u_r^m} & 0 & \dots & 0 \\ \vdots & \vdots & \ddots & \vdots \\ \mathbf{u_r^i} - \mathbf{u_r^m} & 0 & \dots & 0 \\ \mathbf{u_r^1} - \mathbf{u_r^m} & \lambda^1 & \dots & 0 \\ \vdots & \vdots & \ddots & \vdots \\ \mathbf{u_r^i} - \mathbf{u_r^m} & 0 & \dots & \lambda^i \end{bmatrix} \tag{7}$$

where $\mathbf{u_r^*} = \frac{\mathbf{p_r} - \mathbf{p}^*}{D_r^*} = \left[\frac{p_{r,x} - p_x^*}{D_r^*}, \frac{p_{r,y} - p_y^*}{D_r^*}, \frac{p_{r,z} - p_z^*}{D_r^*} \right]$

$\mathbf{x}$ is the state vector including $\mathbf{b} = [b_x, b_y, b_z]$ is the baseline between the rover and reference station ($\mathbf{p}_r = \mathbf{p}_b + \mathbf{b}$) and the float DD ambiguities.

$$\mathbf{x} = [b_x, b_y, b_z, \nabla\Delta N^1, \dots, \nabla\Delta N^i]^T \tag{8}$$

To solve (5) by the least-square estimation, we can find the vector of float solution $\hat{\mathbf{x}}$,

$$\hat{\mathbf{x}} = \mathbf{N}^{-1}\mathbf{A}^T\mathbf{Q}^{-1}\mathbf{y} \tag{9}$$

where $\mathbf{N}$ is the normal matrix calculated by $\mathbf{N} = (\mathbf{A}^T\mathbf{Q}^{-1}\mathbf{A})$. $\mathbf{Q}$ is the cofactor matrix, which is formed by weighting factor of each satellite and its pivot satellite. The weighting factor τ for each satellite can be calculated by [43]. If the carrier-to-noise ratio C/N_0 is larger than a threshold T, then the weighting τ is given as 1, otherwise τ is calculated as

$$\tau = \frac{1}{sin^2 \, el}\left\{ 10^{-\frac{C/N-T}{a}}\left[\left(\frac{A}{10^{-\frac{F-T}{a}}} - 1 \right)\frac{C/N - T}{F - T} + 1 \right] \right\} \tag{10}$$

where el and is the elevation angle of corresponding satellite. T, F, A, a are the constants for controlling the weighting surface. In here, we set T = 50, F = 20, A = 50, a = 30 heuristically. Based on (10), we get two vectors. The first vector contains the i-th available satellite's weighting factor, given that $\mathbf{q_{sat}} = [\tau_r^1 + \tau_b^1, \dots, \tau_r^i + \tau_b^i]^T$. The second vector is the pivot satellite's weighting factor for corresponding i-th available satellite $\mathbf{q_{pivot}} = [\tau_r^m + \tau_b^m, \dots, \tau_r^m + \tau_b^m]^T$, respectively. Noted that these two vectors are both a single column vector with total number of available satellites. Therefore, the cofactor matrix for each satellite and both measurements can be calculated,

$$\mathbf{q} = \mathbf{q_{pivot}}\mathbf{q_{pivot}^T} + diag(\mathbf{q_{sat}})$$
$$\mathbf{Q} = \begin{bmatrix} \mathbf{q} \cdot c_1^2 & \mathbf{0} \\ \mathbf{0} & \mathbf{q} \cdot c_2^2 \end{bmatrix} \tag{11}$$

c_1 and c_2 are the scale factors for pseudorange and carrierphase measurements variance, we set $c_1 = 0.3$ and $c_2 = 0.003$ here. After the float solution $\hat{\mathbf{x}}$ is resolved in (9), with float baseline in ECEF coordinates $\hat{\mathbf{b}}$ and float ambiguities $\hat{\mathbf{a}}$,

the normalized weighted sum of the squared measurement residuals of the LS can be obtained.

$$\hat{\delta}^2 = \frac{(\mathbf{y} - \hat{\mathbf{y}})^T\mathbf{Q}^{-1}(\mathbf{y} - \hat{\mathbf{y}})}{s - u} \tag{12}$$

where s is the total number of observations including code and carrier measurements, which is the size of $\mathbf{y}$. And u is the number of unknowns which is the size of $\hat{\mathbf{x}}$. The $\hat{\delta}^2$ is then multiply to the inverse of the normal matrix $\mathbf{N}^{-1}$ then perform Cholesky factorization, $U = chol(\hat{\delta}^2\mathbf{N}^{-1})$. Finally, the variance-covariance (VC) matrix $\mathbf{C}$ can be obtained,

$$\mathbf{C} = \mathbf{U}^T\mathbf{U} = \begin{bmatrix} \mathbf{Q_{\hat{b}\hat{b}}} & \mathbf{Q_{\hat{b}\hat{a}}} \\ \mathbf{Q_{\hat{a}\hat{b}}} & \mathbf{Q_{\hat{a}\hat{a}}} \end{bmatrix} \tag{13}$$

The float ambiguities $\hat{\mathbf{a}}$ and ambiguity VC matrix $\mathbf{Q_{\hat{a}\hat{a}}}$ will be used for LAMBDA) [19] and will be introduced in the coming sub-section 2). The main goal of ambiguity resolution (AR) is to find an integer vector that can minimize the squared error of LS estimated float ambiguity vector $\hat{\mathbf{a}}$, given that,

$$\min_{\mathbf{a}}\|\hat{\mathbf{a}} - \mathbf{a}\|^2_{\mathbf{Q_{\hat{a}\hat{a}}}^{-1}} \text{ where } \mathbf{a} \in Z^n \tag{14}$$

The integer vector $\mathbf{a}$ with minimum squared vector will be the fixed ambiguities, notated as $\check{\mathbf{a}}$. The fixed ambiguities will then use to find the fixed solution $\check{\mathbf{b}}$.

$$\check{\mathbf{b}} = \hat{\mathbf{b}} - \mathbf{Q_{\hat{b}\hat{a}}}\mathbf{Q_{\hat{a}\hat{a}}}^{-1}(\hat{\mathbf{a}} - \check{\mathbf{a}}) \tag{15}$$

where both fixed ambiguity $\check{\mathbf{a}}$ and fixed solution $\check{\mathbf{b}}$ should be subjected to the minimization constrain.

2) Integer Ambiguity Resolution (AR)
The LAMBDA is introduced in [19, 44] for AR, also implemented in [42]. The main feature of the LAMBDA method is the decorrelation of the ambiguities by Z-transformation, which parameterize the original ambiguities $\mathbf{a}$ to new ambiguities $\mathbf{z} = \mathbf{Z}^T\hat{\mathbf{a}}$.

The VC matrix $\mathbf{Q_{\hat{a}\hat{a}}}$ will first be decomposed into matrices $\mathbf{L}$ and $\mathbf{D}$.

$$\mathbf{Q_{\hat{a}\hat{a}}} = \mathbf{L}^{-T}\mathbf{D}^{-1}\mathbf{L}^{-1} \tag{16}$$

where matrix $\mathbf{D}$ is a diagonal matrix, and matrix $\mathbf{L}$ is a lower triangular matrix. The decorrelation process is to find the transformation matrix $\mathbf{Z}$ which is an integer approximation of $\mathbf{L}$. From [45], by the properties of invertible ambiguity and the integer transformation matrix $\mathbf{Z}$ can be found which equals to $\mathbf{L}$,

$$\mathbf{Q_{\hat{z}\hat{z}}} = \mathbf{Z}^T\mathbf{Q_{\hat{a}\hat{a}}}\mathbf{Z} = \mathbf{Z}^T\mathbf{L}^{-T}\mathbf{D}^{-1}\mathbf{L}^{-1}\mathbf{Z} = \mathbf{D}^{-1} \tag{17}$$

And the estimate $\hat{\mathbf{z}}$ can be found,

$$\hat{\mathbf{z}} = \mathbf{Z}^T\hat{\mathbf{a}} \tag{18}$$

And during the decorrelation process, the VC matrices $\tilde{\mathbf{D}}^{-1}$ and $\tilde{\mathbf{L}}^{-1}$ are updated,

$$\mathbf{Q_{\hat{z}\hat{z}}} = \tilde{\mathbf{L}}^{-T}\tilde{\mathbf{D}}^{-1}\tilde{\mathbf{L}}^{-1}$$
$$\mathbf{Q_{\hat{z}\hat{z}}}^{-1} = \tilde{\mathbf{L}}\tilde{\mathbf{D}}\tilde{\mathbf{L}}^T \tag{19}$$

where the minimization problem for AR in equation (14) becomes,

$$\min_{\mathbf{z}}\|\hat{\mathbf{z}} - \mathbf{z}\|^2_{\mathbf{Q_{\hat{z}\hat{z}}}^{-1}} \text{ with } \mathbf{z} \in Z^n \tag{20}$$

And the decomposition $\tilde{\mathbf{L}}$ and $\tilde{\mathbf{D}}$ in (19) will be used for integer searching with transformed ambiguities.

Noted that the integer searching can be done on original ambiguities $\mathbf{a}$ as well as the transformed ambiguities $\mathbf{z}$. However, the searching will be more efficient with the decorrelated ambiguities [46]. In here, the ambiguities still noted as $\mathbf{a}$ for remaining parts where the ambiguities can be

transformed or not. From (14), we can expend the minimizer to,

$$(\hat{\mathbf{a}} - \mathbf{a})^T \mathbf{Q}_{\hat{\mathbf{a}}\hat{\mathbf{a}}}^{-1} (\hat{\mathbf{a}} - \mathbf{a}) \leq \chi^2 \qquad (21)$$

where χ^2 is a positive value to control the size of the ellipsoidal region [47]. Together with (16), we get,

$$\sum_{i=1}^{I} d_i \left[(a_i - \hat{a}_i) + \sum_{j=i+1}^{I} l_{ji} (a_j - \hat{a}_j) \right]^2 \leq \chi^2 \qquad (22)$$

where d_i is the i-th diagonal element at matrix $\mathbf{D}$. l_{ji} is the element at the j-th row and i-th column at matrix $\mathbf{L}$. (22) shows the integer searching process is done in the sequential conditional adjustment. Where to find the i-th ambiguity a_i, the $(i + 1)$-th up to the end of I-th ambiguities must be conditioned. The whole implementation of integer searching can be found in [42]. Noted that if the ambiguities are transformed at the beginning, a back transformation needs to be done.

$$\breve{\mathbf{a}} = \mathbf{Z}^{-1} \breve{\mathbf{z}} \qquad (23)$$

For different AR approach, the integer set used for baseline coordinate estimation will be different. The AR approaches can be divided into ILS [19] with ratio test [21] and BIE estimator [24].

In this study, the BIE estimator will be used for AR to estimate the ambiguity set. As we believed that the success rate of fixed solution using ILS is not satisfactory in urban areas. For the BIE, the ambiguity set is calculated by the weighted average of the integer set found by LAMBDA [24]. As indicated in [37, 48], the positioning accuracy of BIE is better than that of the float solution of ILS. Meanwhile, BIE can maintain a similar accuracy as the fixed solution of ILS. Unless the special case of a 100% and 0% success rate, their performance will become equal for ILS and BIE estimator [48]. See the calculation of the BIE below.

$$\bar{\mathbf{a}} = \sum_{\mathbf{z} \in \Theta_{\hat{\mathbf{a}}}^{\lambda}} \mathbf{z} \frac{\exp\left(-\frac{1}{2} \|\hat{\mathbf{a}} - \mathbf{z}\|_{\mathbf{Q}_{\hat{\mathbf{a}}\hat{\mathbf{a}}}}^2\right)}{\sum_{\mathbf{z} \in \Theta_{\hat{\mathbf{a}}}^{\lambda}} \exp\left(-\frac{1}{2} \|\hat{\mathbf{a}} - \mathbf{z}\|_{\mathbf{Q}_{\hat{\mathbf{a}}\hat{\mathbf{a}}}}^2\right)} \qquad (24)$$

$$\text{with } \Theta_{\hat{\mathbf{a}}}^{\lambda} = \left\{ \mathbf{z} \in Z^n \mid \|\hat{\mathbf{a}} - \mathbf{z}\|_{\mathbf{Q}_{\hat{\mathbf{a}}\hat{\mathbf{a}}}}^2 < \chi^2 \right\}$$

The BIE estimator obtains the ambiguity set by taking the integer-summation over finite integer set $\mathbf{z}$ inside n-dimension integer space Z^n by tuning the ellipsoidal region constant χ^2, where depends on the float solution and its variance matrix. The weighted average ambiguity set $\bar{\mathbf{a}}$, which equals to $\nabla\Delta\mathbf{N}$ in (2), is then used to calculate the fixed solution with (15).

C. AR and Scoring at Positioning Hypothesis Candidate

After conventional GNSS RTK estimated the initial position in section B, then the 3DMA GNSS RTK will estimate the 'truth visibility' to select the best set of the healthy satellite by distributing a number of hypothesis position candidates around the initial position. On each candidate j, a score will be given based on matchness between the DD carrierphases $\nabla\Delta\boldsymbol{\phi}$ that survived from the skymask aided NLOS exclusion and the simulated DD carrierphases $\nabla\Delta\tilde{\boldsymbol{\phi}}_j$ based on the position candidate j. Theoretically speaking, the candidate with highest score should obtain similar or even identical satellite visibility to the ground truth [49]. This will be discussed in this section. The weighted average candidates based on the given score will be the 'accurate float position' for visibility estimation. Noted that here we name it accurate float position as the ambiguities have not mapped to integer space and it is not the final solution for 3DMA GNSS RTK. Based on the visibility at the accurate

float position, the healthy satellites will be selected to perform GNSS RTK, which will be discussed in section D.

Similar to 3DMA GNSS algorithm [12], hypothesis position candidates are distributed around the initial position by the conventional GNSS RTK in section B. Candidates are distributed with 5m radius with a 50cm resolution. The visibility and ambiguity will be estimated, and the score will be given to the candidate to represent the probability of a candidate being the ground truth or not. Here, the BIE-estimator is selected for the AR at each candidate due to its superiority under noisy measurement [25].

Identical to conventional GNSS RTK, healthy measurement with C/N_0 value larger than 15dB-Hz and elevation angle el larger than 15-degree will be selected. Also, at each candidate P_j, satellites will first perform LOS/NLOS classification with continuous-LOS estimation proposed in [37] to select healthy measurements. In each candidate, the healthy measurements are then passed to AR process, which is similar to the conventional ILS and BIE-estimation in section B.

The survived code and carrier measurements are first double differenced as same as the conventional GNSS RTK. The DD code $\nabla\Delta\rho$ and carrier $\nabla\Delta\phi$ measurements for i-th satellite at j-th candidate can be expressed as,

$$\nabla\Delta\rho_j^i = \nabla\Delta D_j^i + \varepsilon_{\rho_j^i}$$
$$\nabla\Delta\phi_j^i = \nabla\Delta D_j^i + \lambda^i \nabla\Delta N_j^i + \varepsilon_{\phi_j^i} \qquad (25)$$

where $\nabla\Delta N_j^i$ is the ambiguity resolved by the BIE estimator based on the LS estimated float ambiguity $\hat{\mathbf{a}}_j$ at candidate j. The superscript i denotes the index of the common satellite survived from the quality checks ($C/N_0^i > 15\text{dB-Hz}, el^i > 15°$) and skymask aided NLOS exclusion $el^i > el_{skymask,j}(az^i)$. Then, the survived DD measurements are used to LS and estimate the float ambiguities $\hat{\mathbf{a}}_j$ and its VC matrix $\mathbf{Q}_{\hat{\mathbf{a}}\hat{\mathbf{a}},j}$. With the known candidate position $\mathbf{p}_j$, the geometric distance between candidate position $\mathbf{p}_j$ and satellite $\mathbf{p}^i$ yields to,

$$D_j^i = \|\mathbf{p}^i - \mathbf{p}_j\| \qquad (26)$$

Also, the DD geometric distance for LS,

$$\nabla\Delta D_j^i = D_j^i - D_j^m - (D_b^i - D_b^m) \qquad (27)$$

Noted that the DD geometric distance $\nabla\Delta D_j^i$ will also be used together with the resolved integer ambiguity to model the carrierphase and to score the candidate. The DD measurement will obtain the float solution of position $\hat{\mathbf{b}}_j$ and ambiguities $\hat{\mathbf{a}}_j$ at each of the j-th candidate by LS. Total I survived satellite will put into the least square to estimate the float ambiguities $\hat{\mathbf{a}}_j$ as well as VC matrix $\mathbf{Q}_{\hat{\mathbf{a}}\hat{\mathbf{a}},j}$ by (5) to (13) presented in section II.B.1).

After obtaining the float ambiguities $\hat{\mathbf{a}}_j$ and VC matrix $\mathbf{Q}_{\hat{\mathbf{a}}\hat{\mathbf{a}},j}$, we can resolve the integer ambiguity for candidate j. In this paper, the AR process will employ the LAMBDA with BIE-estimator [24] to resolve the ambiguity set. $\mathbf{Q}_{\hat{\mathbf{a}}\hat{\mathbf{a}},j}$ is decomposed and resolve the transformation matrix $\mathbf{Z}_j$ by (16) and (17) respectively. Then the float ambiguities will transform with the transformation matrix with (18) as well as the VC matrix by (19). After that, the LAMBDA method based on (20) to (22) will retrieve several sets of ambiguities inside integer space. The BIE-estimator will be employed to find the weighted

average of integer sets $\boldsymbol{z}$. For the ambiguities at j-th candidate, denoted as $\bar{\mathbf{a}}_j$, is then given as,

$$\bar{\mathbf{a}}_j = \sum_{z \in \Theta} z \frac{\exp\left(-\frac{1}{2}\|\hat{\mathbf{a}}_j - \boldsymbol{z}\|^2_{\mathbf{Q}_{\hat{a}\hat{a},j}}\right)}{\sum_{z \in \Theta} \exp\left(-\frac{1}{2}\|\hat{\mathbf{a}}_j - \boldsymbol{z}\|^2_{\mathbf{Q}_{\hat{a}\hat{a},j}}\right)} \quad (28)$$

$$\text{With } \Theta = \left\{\boldsymbol{z} \in Z^n \mid \|\hat{\mathbf{a}} - \boldsymbol{z}\|^2_{\mathbf{Q}_{\hat{a}\hat{a}},j} < \chi^2\right\}$$

Here, the number of integer set is heuristically set to 100 times of the total number of ambiguities to reduce the computational load.

After the integer ambiguity is resolved, we can obtain the score for the j-th candidate. In (25), the DD carrierphase mainly consists of the DD geometric distance and the DD integer ambiguities. Therefore, we can model the carrierphase after integer ambiguity resolution by,

$$\nabla\Delta\tilde{\phi}_j^i = \nabla\Delta D_j^i + \lambda^i \bar{a}_j^i \quad (29)$$

The score for the j-th candidate S_j can be obtained by the mean square error between measurements and modelled carrierphase based on the Gaussian noise assumption. In theory, after the exclusions, only healthy measurements are remained and the likelihood should follow the Gaussian distribution [50].

$$S_j = \exp\left[-0.5 \times \frac{1}{I} \sum_{i=1}^{I} \left(\nabla\Delta\phi^i - \nabla\Delta\tilde{\phi}_j^i\right)^2\right] \quad (30)$$

where I is the total number of survival satellites after exclusion. Noted that in the $\left(\nabla\Delta\phi^i - \nabla\Delta\tilde{\phi}_j^i\right)$, if the candidate is closer to the ground truth, the value of $\nabla\Delta D_j^i$ will be close to the measurement $\nabla\Delta\phi^i$ itself. As a result, the better integer ambiguity $\bar{a}_j^i$ can be obtained to describe the carrierphase measurements $\nabla\Delta\phi^i$. In other words, a smaller value of $\left(\nabla\Delta\phi^i - \nabla\Delta\tilde{\phi}_j^i\right)$, as well as the mean square error (MSE) $\frac{1}{I}\sum_{i=1}^{I}\left(\nabla\Delta\phi^i - \nabla\Delta\tilde{\phi}_j^i\right)^2$, a higher score will be given, as shown in the heatmap of Fig. 2(a).

D. 3DMA GNSS RTK

After scoring each candidate, the accurate float position (3DMA HYPO with the light blue point in Fig. 2(b)) can be found by weighted averaging the candidate $\mathbf{p}_j$ with their score S_j, where there are total J positioning candidates.

$$\mathbf{p}_{3DMA} = \frac{\sum_{j=1}^{J} S_j \times \mathbf{p}_j}{\sum_{j=1}^{J} S_j} \quad (31)$$
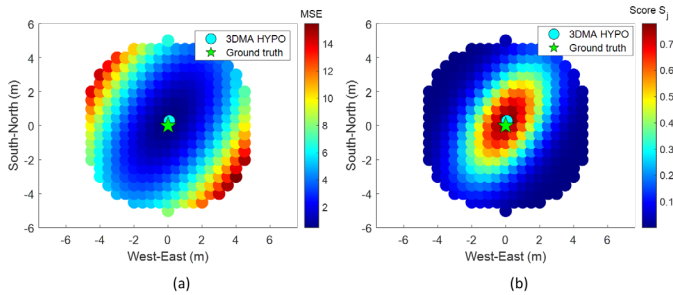
Fig. 2. Heatmap on (a) mean square error (MSE) of position hypothesis candidates, smaller or bluish the better; and (b) score of position hypothesis candidates calculated by (30), larger or reddish the better. Green star: ground truth; Light blue point (3DMA HYPO): position hypothesis solution calculated by (31).

At the accurate float position $\mathbf{p}_{3DMA}$, the AR with BIE-estimator will be done once again to refine the positioning result. It means the $\mathbf{p}_{3DMA}$ plays a role in providing accurate float solution to the AR. GNSS RTK with satellite visibility at $\mathbf{p}_{3DMA}$ will be performed once again, which is the same as what have done in (25) but replacing $\mathbf{p}_j$ with $\mathbf{p}_{3DMA}$. The NLOS exclusion and continuous-LOS estimation will be performed based on the hypothesis position solution $\mathbf{p}_{3DMA}$. Identical to the conventional RTK positioning, float solution of position $\hat{\mathbf{b}}_{3DMA}$, ambiguities $\hat{\mathbf{a}}_{3DMA}$, and VC matrix $\mathbf{Q}_{\hat{a}\hat{a},3DMA}$ are obtained by the least square method same as section B.1). Then the AR process with BIE-estimator is performed by inputting $\hat{\mathbf{a}}_{3DMA}$ and $\mathbf{Q}_{\hat{a}\hat{a},3DMA}$. By following (17) to (24), the BIE will estimate the ambiguities $\bar{\mathbf{a}}_{3DMA}$ by weighted average all integer sets with its MSE,

$$\bar{\mathbf{a}}_{3DMA} = \sum_{z \in \Theta} z \frac{\exp\left(-\frac{1}{2}\|\hat{\mathbf{a}}_{3DMA} - \boldsymbol{z}\|^2_{\mathbf{Q}_{\hat{a}\hat{a},3DMA}}\right)}{\sum_{z \in \Theta} \exp\left(-\frac{1}{2}\|\hat{\mathbf{a}}_{3DMA} - \boldsymbol{z}\|^2_{\mathbf{Q}_{\hat{a}\hat{a},3DMA}}\right)} \quad (32)$$

$$\text{With } \Theta = \left\{\boldsymbol{z} \in Z^n \mid \|\hat{\mathbf{a}} - \boldsymbol{z}\|^2_{\mathbf{Q}_{\hat{a}\hat{a}}} < \chi^2\right\}$$

And the final 3DMA GNSS BIE RTK solution $\bar{\mathbf{b}}_{3DMA}$ as,

$$\bar{\mathbf{b}}_{3DMA} = \hat{\mathbf{b}}_{3DMA} - \mathbf{Q}_{\hat{b}\hat{a},3DMA}\mathbf{Q}^{-1}_{\hat{a}\hat{a},3DMA}(\hat{\mathbf{a}}_{3DMA} - \bar{\mathbf{a}}_{3DMA}) \quad (33)$$

After mapping the ambiguities from real numbers $\hat{\mathbf{a}}_{3DMA}$ to integer one $\bar{\mathbf{a}}_{3DMA}$ with BIE estimator, the fixed baseline solution $\bar{\mathbf{b}}_{3DMA}$ can be obtained.

After discussing the details of both the conventional GNSS RTK and proposed 3DMA GNSS RTK, it is followed by the designed experiment in the urban environment to demonstrate the performance of 3DMA GNSS RTK and evaluate how satellite selection is important to GNSS RTK in section III.

III. POSITIONING PERFORMANCE AND ANALYSIS

A. Experiment Setup

Several experiments were conducted in different suburban and urban canyons in Hong Kong, as shown in Fig. 3(a). Table I summarises the experiments' information. The calculation of the mean and STD of the elevation angle of the skymask can be found at [51]. Skymask at the locations of Experiments 1-5 with available satellites are shown in Fig. 3(b)-(f), respectively. The measurements were collected using the commercial-grade u-blox F9P and geodetic grade NovAtel FlexPak6. A NovAtel GPS-702-GG active antenna was employed and connected to two receivers with a splitter to have a common-ground on the received signals, as shown in Fig. 4. The reference station of Hong Kong Satellite Positioning Reference Station Network (SatRef) does not provide the GALILEO data for post-processing. Thus, only GPS (L1 and L2) and BeiDou (B1 and B2) are used in the evaluation.

We modified the open-source code goGNSS [52] to implement the proposed method in this paper for the evaluation. The skymask for satellite visibility estimation is pre-generated from the 3D building model. The 3D building model is provided by the Lands Department of Hong Kong. According to their quantitative positional accuracy assessment results provided, the horizontal and vertical positional accuracy for buildings is 1m, and for terrain model is 2m. In this study, the 3D building

model is only used for NLOS satellite exclusions, the accuracy will not affect the classification accuracy much. In [5] proposed, when the uncertainty of building model increased to 8m, the visibility classification can still achieve 95.47%.
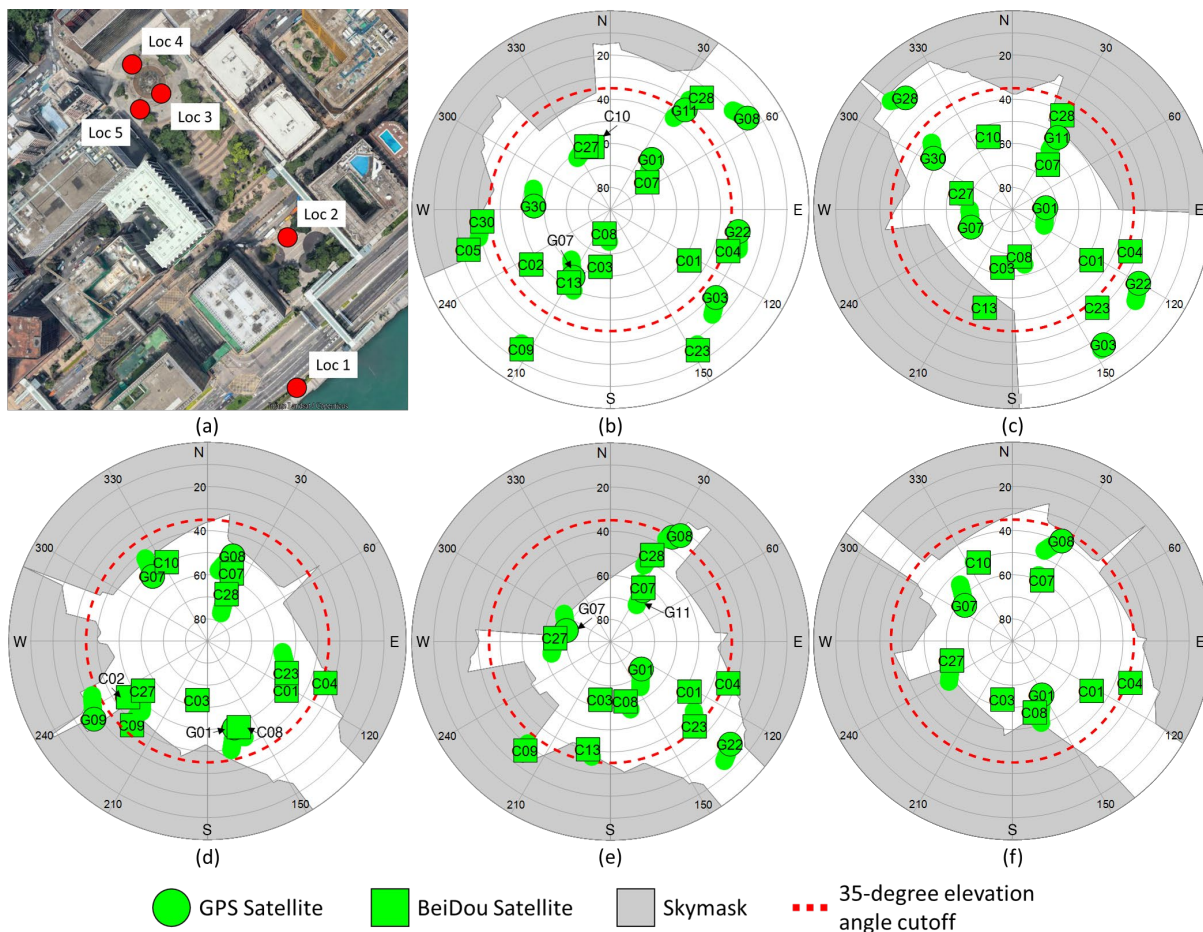
Fig. 3. (a) Experiment locations in Hong Kong urban areas. (b)-(f) Skymask at experiment locations 1-5, respectively.

TABLE I
EXPERIMENT INFORMATION

Location	Number of epochs (at 1Hz output rate)	Scenario	Skymask elevation angle mean (degree)	Skymask elevation angle STD (degree)	Skymask Maximum elevation angle (degree)
1	900	Opensky	11.1	14.9	42.0
2	900	Suburban	30.6	21.0	55.9
3	1200	Urban	36.9	12.8	51.7
4	1200	Urban	43.2	17.9	67.6
5	900	Urban	37.8	15.7	58.3

Fig. 4. Experiment equipment.
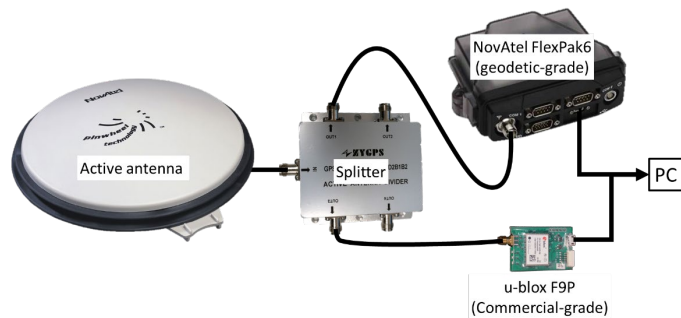
B. *Ground Truth Determination and Variation*

As the required positioning accuracy of this study is in centimetre-level, therefore, the determination of experiment ground truth is important. When doing the experiment, the RTK estimated by NovAtel Flexpak 6 is performed at the same time to get the average best position as the ground truth. For RTK, the Hong Kong SatRef service by Hong Kong Land Department is employed. Reference station 'HKSC' is selected for the short baseline double differencing, where the geometric distance is

about 4.6 km to the experiments' location averagely. Before start recording the raw measurement for both receivers, we wait until the NovAtel receiver to resolve the position type on narrow integer solution ('NARROW_INT' output), which is multi-frequency RTK solution with carrierphase ambiguities resolved to narrow-lane integers. After the narrow-lane solution are obtained about one-minute, we start to record the raw measurements for both receivers while the NovAtel keeps outputting the RTK solution.

At the post-processing stage, all the resolved narrow-lane integers RTK solution will be extracted and taking average as the ground truth. The validation between ground truth and all narrow-lane solutions for all experiment are summarised in Table II.

TABLE II
GROUND TRUTH INFORMATION ESTIMATED BY NOVATEL FLEXPAK 6. STD STANDS FOR STANDARD DEVIATION.

Experiment	No. of position output (at 1Hz)	Percentage of narrow-lane solution	Maximum 2D error (cm)	Minimum 2D error (cm)	Mean 2D error (cm)	STD of 2D error (cm)
1	986	95.9%	1.86	0.60	1.00	0.41
2	967	97.6%	3.64	0.37	1.18	0.66
3	1321	99.6%	2.56	0.37	0.93	0.50
4	1005	99.4%	4.25	0.43	1.33	0.77
5	1292	80.0%	2.56	0.37	0.93	0.50

The average difference between calculated ground truth and all narrow-lane position is about 1cm with a standard deviation (STD) about 0.5cm. The calculated position is used as the ground truth to evaluate the RTK performance of different algorithms. However, it is hard to determine which algorithm performs better theoretically if the positioning difference between two algorithms is within 1cm.

C. ADOP Value and Positioning Performance

In theory, after performing the 3DMA exclusion, only the healthy satellites are used to AR process for RTK positioning. In other words, the ambiguity dilution of precision (ADOP) value should be decreased. The ADOP is proposed in [53], representing the precision of the float ambiguities. The more precise the float ambiguities is, the higher the probability of estimating the correct integer ambiguities is. ADOP is an easy-to-evaluate scalar precision measure that calculated by the determinant of the float ambiguity VC-matrix, $\mathbf{Q}_{\hat{a}\hat{a}}$, and its dimension, n,

$$ADOP = |\mathbf{Q}_{\hat{a}\hat{a}}|^{1/2n} \quad \text{[unit: cycle]} \quad (34)$$

The value of ADOP = 0.12 cycles, usually as a rule of thumb for the ambiguity success rate of 99.9% [54]. In here, we will compare the ADOP and PDOP values on with and without adopting 3DMA method for the BIE and 3DMA GNSS RTK, which is the proposed method of this study. Table III summarises the average ADOP and PDOP of all experiments. The PDOP and ADOP of 3DMA GNSS RTK are obtained based on the 3DMA NLOS exclusion at ground truth location, labelled as 3DMA BIE@GT.

TABLE III
AMBIGUITY DILUTION OF PRECISION (ADOP) AND POSITION DILUTION OF PRECISION (PDOP) OF EACH EXPERIMENT

Experiment	Average ADOP (cycle)		Average PDOP	
	BIE	3DMA BIE@GT	BIE	3DMA BIE@GT
1	0.03	0.03	0.99	1.00
2	0.49	0.06	1.36	1.44
3	0.05	0.05	2.01	2.03
4	0.32	0.06	1.46	1.57
5	0.21	0.11	3.75	4.19

From the results shown in Fig. 5, a large 2D positioning error can be found for the BIE, especially for the large ADOP value at the beginning to about 200s. The positioning error can achieve over 10m with ADOP value exceeds 1 cycle. Besides, it can be observed that the ADOP value is decreased after applying 3DMA GNSS, with originally over 1 cycle, and decreased to within 0.2 cycles. While the PDOP value only increases a bit after the 3D building model is used to exclude the NLOS measurements, where PDOP value with 3DMA only about 0.2 larger than that of the BIE. And maximum PDOP value with 3DMA is about 2 at about 500s, which is 0.5 larger than that of BIE. After satellite exclusions, the low ADOP value should obtain a good RTK positioning results theoretically; however, not all results show the same phenomena. For example, the marked point at 842s in Fig. 5. The ADOP and PDOP value are 0.06 and 1.30, respectively. However, the 2D positioning error is larger over 2m here. This may cause by the noise from the multipath effects that contribute to the carrierphase measurements. Furthermore, at about epoch 500, a large number of satellites are excluded by 3DMA, and the PDOP increased to about 3 for the 3DMA method, while PDOP is 2 for the BIE. However, ADOP value does not increase much here. And the positioning result does not increase at the same time.
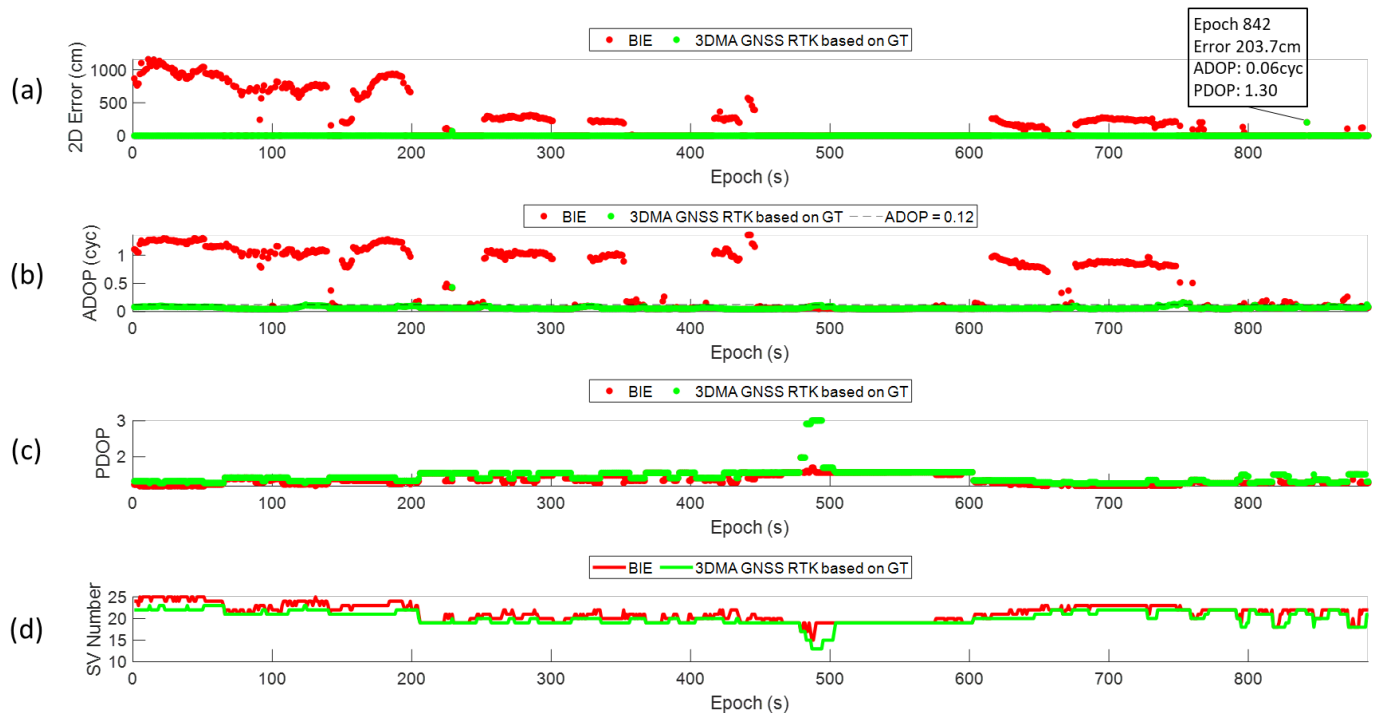
Fig. 5. (a) Positioning error, (b) ADOP value, (c) PDOP value, and (d) number of satellite (SV) on the 3DMA BIE@GT (green) and BIE (red) of experiment 2.

This result shows that even though the PDOP value of BIE is low, the ADOP value is high, the RTK positioning error is still large. Which means the noisy measurements are contributing to the AR and degrade the positioning performance. After applying the 3DMA, only the healthy measurements remain, and they are precise enough to resolve ambiguity set for the RTK solution.

D. Positioning Results

In this section, the post-processed results will be analysed and compared by different positioning algorithms, including:

1) BIE
Position with AR by BIE estimator.

2) BIE@EL35
The position with AR by BIE estimator, increases the mask elevation angle to 35-degree. This method is selected because many of the existing works adopt high elevation angle mask assumption in urban GNSS RTK [55].

3) 3DMA BIE RTK
The position with AR by BIE estimator, and visibility estimation at accurate float position with 3DMA exclusion, which is the proposed method.

4) 3DMA BIE@GT (Theoretically the best)
The position with AR by BIE estimator, visibility estimation at ground truth and 3DMA exclusion. This method is theoretically the best solution, as both the initial state and visibility are both estimated at ground truth location.

The initial state estimation method, AR method, and other satellite selection parameters are shown in Table IV. The elevation cut-off angle and C/N_0 thresholds are empirical constant. This value could be diverse for different measurement frequencies, constellation, and equipment setup. The constant for continuous-LOS estimation is same as the value in [37], where GPS is set to 6s and BDS is set to 15s. And the first 6s will not exclude any satellite until the starting to exclude the GPS satellite.

TABLE IV
POST-PROCESSING INFORMATION AND PARAMETERS FOR DIFFERENT ALGORITHMS

Algorithm	Initial state estimation	AR method	Usage of 3D models	Applying continuous LOS (C-LOS)	Elevation cutoff angle (degree)	C/N0 cutoff (dB-Hz)
BIE	Least square	BIE	No	No	15	
BIE@EL35	Least square	BIE	No	No	35	
3DMA BIE RTK	Accurate float position	BIE	Yes	Yes	15	15
3DMA BIE@GT	Ground truth	BIE	Yes	Yes	15	

The positioning results of Experiments 1 to 5 by the geodetic-grade receiver are summarized in Table V. The 2D positioning error statistic are categorised in root-mean-squared (RMS) error, mean error, standard deviation (STD), maximum

(Max) error, and minimum (Min) error.

TABLE V
2D POSITIONING ERROR SUMMARY ON EXPERIMENTS 1 TO 5 BY GEODETIC-GRADE RECEIVER (UNIT: CM)
BIE: RTK GNSS SOLUTION WITHOUT 3DMA. BIE@EL35: INCREASE THE ELEVATION CUTOFF ANGLE TO 35 DEGREES TO EXCLUDE SATELLITE.
3DMA BIE RTK: PROPOSED METHOD OF THIS STUDY. 3DMA BIE@GT: 3DMA EXCLUSIONS WITH PERFECT CASE.

Experiment		BIE	BIE@EL35	3DMA BIE RTK	3DMA BIE@GT
1	RMS	1.15	1.50	1.15	1.15
	Mean	1.02	1.36	1.03	1.03
	STD	0.53	0.63	0.53	0.53
	Max	2.33	2.77	2.33	2.33
	Min	0.03	0.02	0.03	0.03
2	RMS	382.83	306.86	7.47	7.47
	Mean	214.33	135.43	1.91	1.91
	STD	317.39	275.51	7.22	7.22
	Max	1157.70	885.38	203.68	203.68
	Min	0.22	0.14	0.03	0.03
3	RMS	0.90	0.95	0.93	0.95
	Mean	0.78	0.86	0.82	0.84
	STD	0.44	0.41	0.45	0.45
	Max	2.09	1.97	2.09	2.09
	Min	0.01	0.02	0.01	0.01
4	RMS	241.76	30.11	7.95	8.11
	Mean	126.78	10.31	1.76	2.16
	STD	205.96	28.30	7.75	7.82
	Max	593.57	195.78	124.25	124.25
	Min	0.08	0.06	0.05	0.01
5	RMS	216.85	62.02	1.93	1.93
	Mean	74.46	23.43	1.37	1.37
	STD	203.75	57.45	1.37	1.37
	Max	1201.26	295.91	28.00	28.00
	Min	0.03	0.03	0.03	0.03

In the first experiment, it locates in a relatively openksy area, most of the satellites are the LOS ones. Therefore, the 3DMA cannot help the positioning by excluding the NLOS satellite, and their PDOP value are nearly the same. As a result, the positioning performance is identical for RTK GNSS with and without aiding of the 3D building model, which are BIE and 3DMA BIE RTK, the RMS positioning error is about 1cm and maximum positioning error is about 2cm. However, for the BIE@EL35, a larger positioning error is obtained. The RMS error increases to 1.5cm, with the largest position error near 3cm. The average ADOP and PDOP value of BIE@EL35 are 0.04 and 2.76, respectively. The ADOP value is similar to that of BIE, but the PDOP value is worst, resulting in a larger positioning error.

The second experiment locates in the suburban environment which is in between two buildings. The positioning RMS error of BIE is about 4m, while there is still about 3m RMS error for BIE@EL35. The 3DMA BIE RTK positioning results achieve the RMS error within 10cm while the largest error is about 2m. Furthermore, it is identical to the theocratically best result, which is 3DMA BIE@GT. This implies this error could be caused by multipath effects, which currently cannot be identified by 3D models.

The cumulative distribution function (CDF) of the 2D positioning error of Experiment 2 is shown in Fig. 6. From the meter-level accuracy CDF plot, we can observe that the 2D positioning error of 3DMA BIE RTK is far smaller than that of

BIE. Looking at the centimetre-level CDF plot, BIE only achieves about 60% of data positioning error that is within 10cm. After increasing the elevation cut-off angle to 35-degree, it is increased to about 80%. After applying 3DMA, near all epoch positioning error is within 10cm. This result shows that increasing the elevation cut-off angle can improve the positioning performance to a certain extent, while 3DMA GNSS RTK can improve performance dramatically in the urban environment.
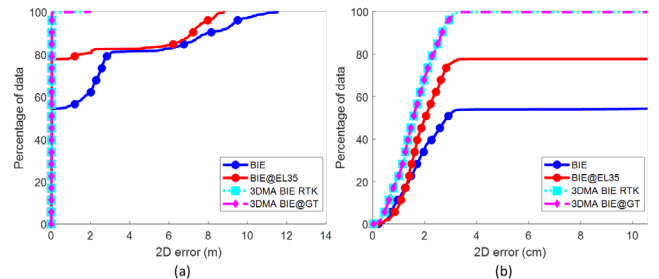
Fig. 6. Cumulative distribution function (CDF) of the 2D positioning error of experiment 2 in (a) metre-level and (b) centimetre-level.

The third experiment locates in an urban environment surrounded by three buildings. Although the location of Experiment 3 is with severe NLOS and multipath effects, BIE and BIE@EL35 are still able to achieve a good result. All

algorithms perform well, and the RMS error is within 1cm while the maximum error is about 2cm. The reason for this good positioning in this urban environment is the good ADOP value for all available satellites. From Table III, we can see that the average ADOP for experiment 3 of BIE is 0.05, which is similar to that of Experiment 1 (opensky). Therefore, even the PDOP value of experiment 3 of BIE is 2.01, the low ADOP value can still achieve a good RTK positioning. In this experiment, although a smaller RMS and mean error are found in BIE, we cannot conclude that BIE is outperformed others. As the difference between each value is within 0.05cm where the mean difference of experiment 3 ground truth is near 1cm with a standard deviation of 0.5cm, and the maximum difference is about 2.5cm.

Experiments 4 and 5 located near the buildings, therefore, the skymask at these two locations are non-evenly distributed. In other words, a higher elevation cut-off angle (BIE@EL35 solution) does not help the positioning results as much compared with the proposed 3DMA GNSS RTK. 3DMA BIE RTK outperforms BIE@EL35 more than 20cm on RMS error for both experiments.

In Experiment 4, the RMS positioning error of BIE is in the meter-level where the positioning RMS error is about 2.4m. after increasing the elevation cut-off angle, the positioning error reduced to about 30cm. In here, the 3DMA BIE RTK perform the best that RMS error is about 8cm with maximum positioning error for about 1.2m. Although from the value 3DMA BIE RTK is smaller than that of 3DMA BIE@GT on RMS and mean error, we cannot conclude the 3DMA BIE RTK outperforms. But it is definitely 3DMA BIE RTK achieve similar performance to the theoretically the best result (3DMA BIE@GT).

For Experiment 5, a similar improvement in 3DMA can be found. The BIE obtains an RMS error over 2m. BIE@EL35 can reduce the RMS error to within 1m, to about 60cm. With the 3DMA, the RMS error reduces dramatically to within 2cm, where maximum positioning error is about 28cm. This result is identical to the theoretically the best result.

The summary of the positioning error of 3DMA GNSS RTK shown in Fig. 7. After applying the 3D building model, 75% of error is within 2.5cm, and only a few outliers can be found. Also, the summary of 3DMA GNSS RTK improvement shows in Table VI. In here, only the epoch with smaller positioning error by 3DMA GNSS RTK is found to be considered as 'improved epoch'. In urban environments like experiment 2, 4, and 5, more than half of the epoch are improved and reduce the positioning error with more than 1m averagely. Even on the opensky environment like experiment 1, 3DMA GNSS is not expected to perform well, but an improvement of 40% epochs in observed.
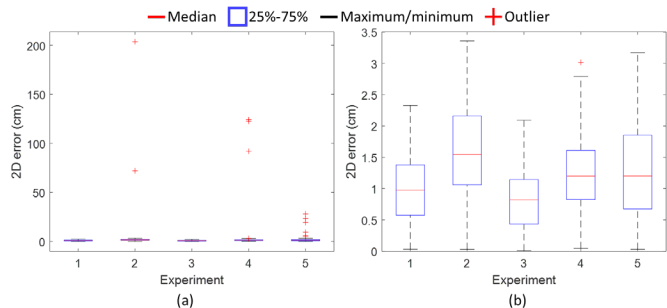
Fig. 7. (a) Box plot on 3DMA BIE RTK in different experiments. (b) zoom in of (a) to centimetre-level.

TABLE VI
SUMMARY OF POSITIONING ERROR IMPROVEMENT PERCENTAGE AND THE AVERAGE VALUE. ONLY THE EPOCH WITH SMALLER POSITIONING ERROR BY 3DMA GNSS RTK IS FOUND TO BE CONSIDERED AS IMPROVED.

Experiment	Percentage on improved epoch (%)	Average 2D improvement (cm)
1	40.52	0.0025
2	79.46	267.38
3	32.80	0.06
4	57.79	216.42
5	56.83	128.89

RTK positioning in urban required good quality of carrierphase measurement. Up to here, we have shown the 3DMA GNSS RTK can perform well in the urban area with the raw measurement by the geodetic-grade receiver. However, a different story is told by a commercial-grade receiver, where the measurement quality is relatively poor. As well as receiving the noisy measurements in an urban environment, the positioning results are bad. The positioning results for the u-blox F9P are summarised in Table VII. The RTK positioning results for the commercial-grade receiver is large compared to a geodetic-grade receiver. This could be due to the receiver noise with bad measurement quality (coming from the characteristic of the high-sensitivity), results in large position error.

TABLE VII
SUMMERY ON POSITIONING RESULTS BY U-BLOX F9P RECEIVER (UNIT: CM)
BIE: RTK GNSS SOLUTION WITHOUT 3DMA. BIE@EL35: INCREASE THE ELEVATION CUTOFF ANGLE TO 35 DEGREES TO EXCLUDE SATELLITE.
3DMA BIE RTK: PROPOSED METHOD OF THIS STUDY. 3DMA BIE@GT: 3DMA EXCLUSIONS WITH PERFECT CASE.

Experiment		BIE	BIE@EL35	3DMA BIE RTK	3DMA BIE@GT
1	RMS	163.24	162.61	163.24	163.24
	Mean	136.08	134.45	136.08	136.08
	STD	90.21	91.52	90.21	90.21
	Max	335.98	394.53	335.98	335.98
	Min	0.61	1.35	0.61	0.61
2	RMS	268.41	349.87	162.72	204.76
	Mean	184.38	185.88	98.54	120.92
	STD	195.17	296.57	129.57	165.34

	Max	1267.36	1723.07	1154.68	1154.68
	Min	0.46	0.05	0.05	0.05
3	RMS	109.43	115.90	107.94	107.53
	Mean	91.49	100.54	90.74	90.33
	STD	60.07	57.68	58.49	58.36
	Max	272.46	309.98	272.46	272.46
	Min	0.42	0.43	0.42	0.42
4	RMS	131.74	129.68	130.66	161.18
	Mean	115.85	111.96	107.46	128.57
	STD	62.76	65.49	74.37	97.27
	Max	294.53	282.54	303.96	615.60
	Min	0.84	1.19	0.52	0.79
5	RMS	90.48	91.65	210.95	86.54
	Mean	73.45	74.56	90.16	72.01
	STD	52.86	53.31	190.80	48.03
	Max	245.74	245.74	3086.53	233.46
	Min	0.25	0.25	0.25	0.25

Due to the noisy measurements, the commercial-grade receiver can only provide a metre level accuracy RTK positioning. However, the 3DMA BIE RTK can still improve the positioning accuracy on most of the case. However, a large positioning error found in experiment 5 due to the wrong satellite exclusion. In here, we use one of the epochs to explain the reason, which is shown in Fig. 8.
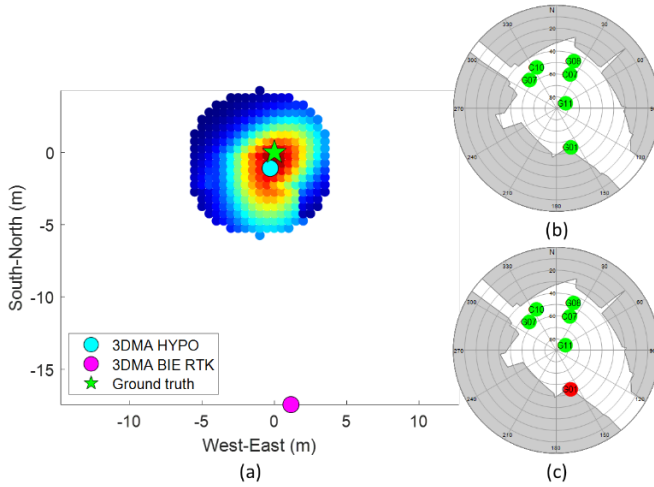
Fig. 8. (a) position heatmap. (b) skymask at ground truth with available satellites. (c) skymask at 3DMA HYPO (accurate float position) with available satellites. NOTE: green circle represents the satellite used for RTK, red circle represents excluded satellite.

As the proposed 3DMA BIE RTK uses the visibility at accurate float position (light blue point in Fig. 8(a)) for the AR process. The position hypothesis solution obtains about 1.14m error, and accidentally excluded the G01 satellite with both L1- and L2-band measurements (as shown in Fig. 8(c)). However, the G01 should be a LOS satellite at ground truth and should not be excluded. This exclusion results in the PDOP value is increased from 4.7 to 18.0, and comparing MSE of the ambiguity set by BIE estimator between 3DMA BIE RTK and 3DMA BIE@GT, the values are 0.3332 and 0.1075, respectively. The larger MSE value implies that the estimated ambiguity set of 3DMA BIE RTK is possibly not optimal. As a result, the position error increases to about 17.5m. The result shows that an accurate visibility estimation location is also important to the 3DMA GNSS RTK.

E. Positioning Results using 3-Hours of Data

A 3-hours static experiment is also conducted in Location 3 to validate the developed 3DMA GNSS RTK. The equipment setup is identical to the description in section III.A. The 2D positioning error, ADOP, PDOP, and received satellite numbers are shown in Fig. 9. The overall positioning performance is summarised in Table VIII.
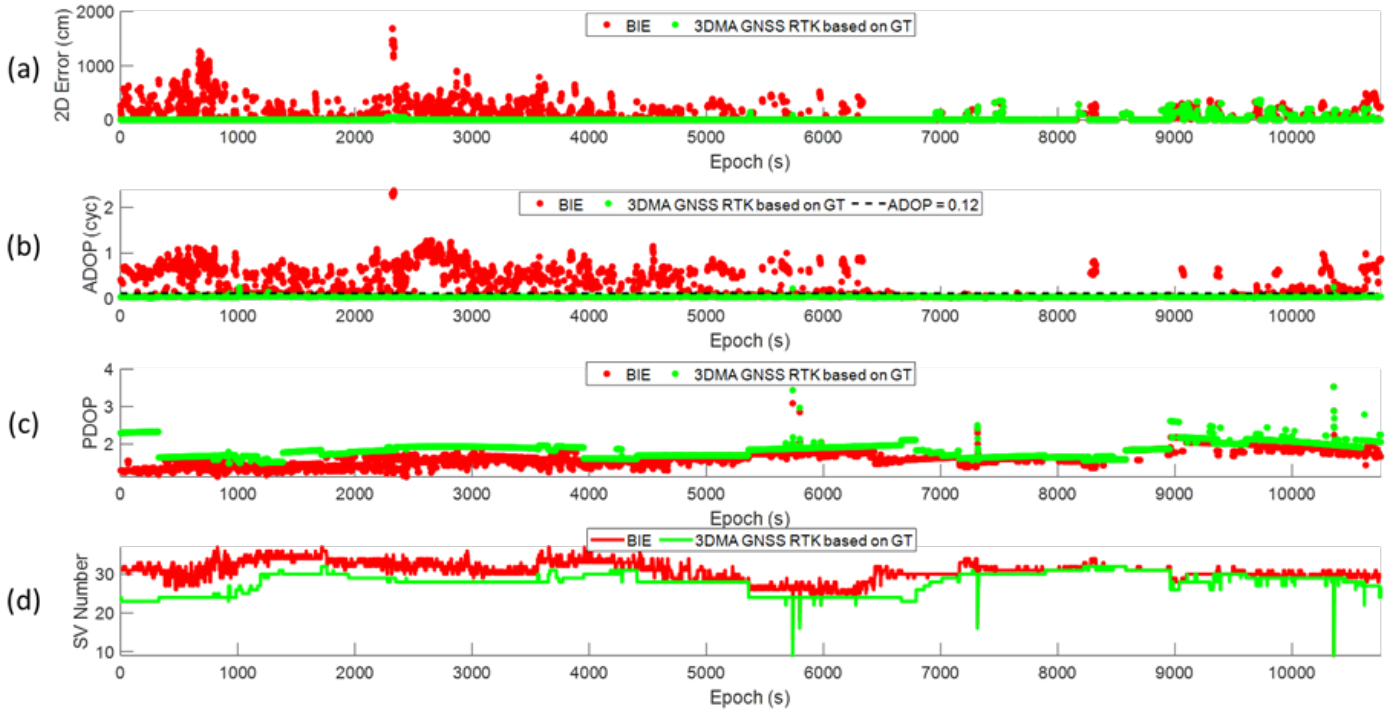
Fig. 9. Comparison on BIE and 3DMA BIE RTK on (a) 2D positioning error, (b) ADOP value, (c) PDOP, and (d) number of satellite (SV) received.

	BIE	BIE@EL35	3DMA BIE RTK	3DMA BIE@GT
RMS	180.59	109.07	49.05	48.54
Mean	82.66	45.48	14.94	14.70
STD	160.57	99.14	46.72	46.26
Max	1689.80	774.00	369.42	353.07
Min	0.02	0.03	0.02	0.02

Comparing the ADOP and PDOP values, although the PDOP value of the 3DMA method increased, the ADOP value is decreased compared to the conventional BIE. The results show that the 3DMA excludes the unhealthy satellites successfully, and only the good measurements are used for the AR. The BIE@EL35, the 2D RMS error is about 1m with maximum positioning error about 8m. After applying 3D models, the RMS error of 3DMA BIE RTK is near half metre only. The result here is also nearly the same as theoretically the best result, 3DMA BIE@GT. Especially in the first half experiment time period (1 to about 6,000 epochs), the proposed method excluded a lot of satellites, and the PDOP increased from 1.3 to nearly 2.0. However, the satellite exclusions can improve the ambiguity precision much, this can be observed from the change of ADOP value. The ADOP value decreased much from about 0.5 to 0.04. As a result, the 2D positioning result improved.

The accuracy of accurate float position is the key to affect the visibility estimation for 3DMA BIE RTK. An incorrect visibility estimation can bring an incorrect AR, resulting in a degraded positioning performance. The 2D positioning error of accurate float position ($\mathbf{p}_{3DMA}$ in (31)) in and 3DMA BIE RTK is shown in Fig. 10 (a). The percentage of visibility classification correctness Fig. 10 (b). We assume the visibility estimation is correct at the ground truth, and we compare to it at the accurate float position to obtain the correctness percentage of the visibility classification.
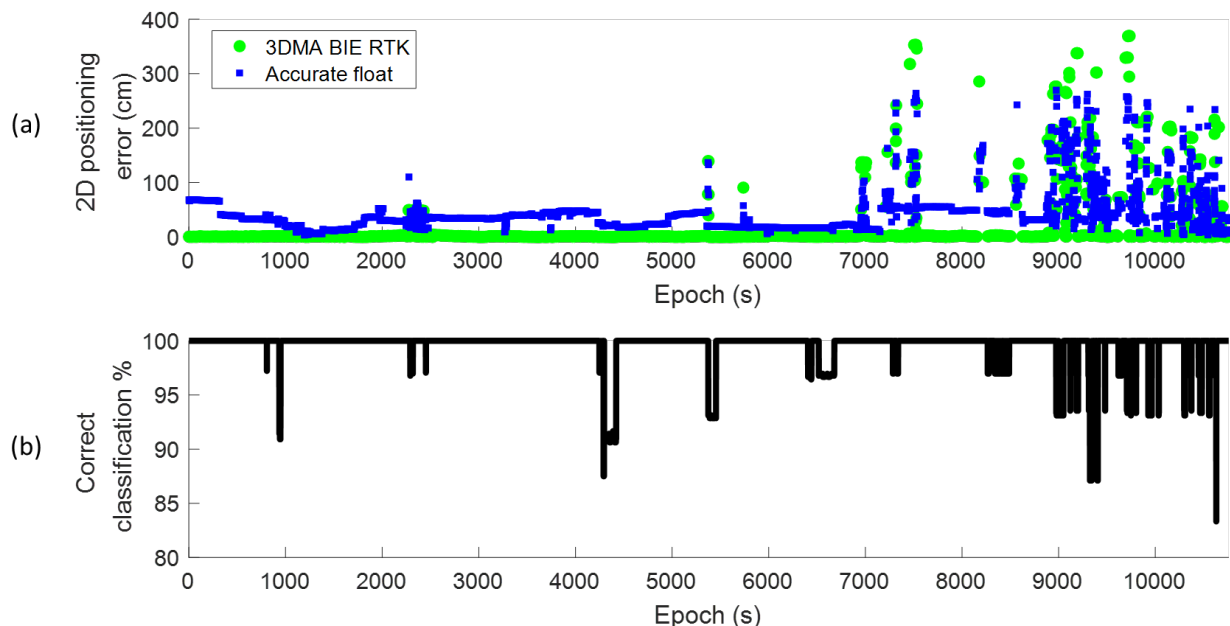
Fig. 10. (a) 2D positioning error of accurate float position, $\mathbf{p}_{3DMA}$ in (31), and 3DMA BIE RTK. (b) Correctness of the visibility estimation between that based on the accurate float position and ground truth.

At the first half of the experiment, nearly all 2D positioning errors of accurate float position are within 1m, and 3DMA BIE RTK can obtain a good positioning result. After epoch 7000, the error of accurate float position fluctuates rapidly, and the average error increases to over 1m. And the classification percentage start decreasing at the same time, which means the unhealthy measurements could be used for the AR in 3DMA BIE RTK. We can observe that the performance become worse after epoch 7000, the 2D positioning error increased over 1m for several numbers of epochs.

F. Computation Load Evaluation

This study has shown that 3DMA RTK GNSS can improve RTK GNSS positioning in urban canyon. However, the required computation load is a crucial factor for real-time applications. Table IX shows the average duration required to output one positioning solution for the two methods.

TABLE IX
COMPUTATIONAL LOAD FOR THE BIE AND 3DMA BIE RTK.

	BIE	3DMA BIE RTK
Average duration for one epoch solution (s)	0.10	21.94
Average number of available satellites	31	23

The conventional method, BIE, only uses 0.1s to output position solution while proposed 3DMA BIE RTK uses about 22s. The main computational load of proposed method goes to the AR at each positioning candidate, sampling all candidates using about 21.8s in total. At the same time, obtaining final positioning used about 0.1s, which is same as BIE. To conclude, the accurate float position estimation is currently computationally intensive, making 3DMA GNSS RTK hard to implement for real-time application.

IV. CONCLUSIONS AND FUTURE WORK

In this study, a novel 3DMA GNSS RTK positioning algorithm is proposed. The 3DMA GNSS RTK uses the hypothesis position candidates for NLOS exclusions and selects the healthy satellites for ambiguity resolution. The positioning accuracy can be improved compared to conventional RTK positioning. Nevertheless, the analysis also shows that the NLOS exclusion by skymask is important for RTK in urban areas compared to that uses a fixed elevation cut-off angle. This advantage is obvious when the RTK receiver is located in the urban environment with non-uniform building distribution. Experiment results show that the satellite exclusion will slightly increase the PDOP value, while the ADOP value will remain the same or decrease dramatically. In other words, a correct satellite exclusion can benefit the AR for RTK positioning by increasing the probability of resolving the correct ambiguities, which is the key for RTK positioning. 3DMA GNSS RTK can perform RTK positioning in urban with accuracy within 10cm averagely with the geodetic grade receiver.

Currently, the hypothesis candidates with ambiguity searching are used to find the accurate float position for visibility estimation. There are two main limitations to this method. The first limitation is the hypothesis candidates need to cover the ground truth location to ensure the correct visibility can be examined. The second limitation is the intensive computational load of the proposed method. These limitations make it difficult to implement the 3DMA GNSS RTK practically. Therefore, the evaluation process will soon be replacing with gradient-descent methods to reduce the computation load, such as Newton's method to resolve the best position iteratively for visibility estimation.

Besides, this paper only shows the feasibility of 3DMA GNSS RTK with a static experiment. In the near future, more experiment will be done in a different urban environment as well as the driving experiment to show the performance of 3DMA GNSS RTK in the urban environment. Also, the cycle slip detection and correction scheme need to be added to improve the healthy satellite selection for the 3DMA GNSS RTK as cycle slip is one of the most common errors for the urban RTK. Furthermore, if the commercial-grade receiver is not feasible to perform RTK positioning in the urban environment, another satellite weighting scheme or satellite selection method must be performed to achieve urban RTK positioning.

REFERENCES

[1] J. Moreau, S. Ambellouis, and Y. Ruichek, "Fisheye-Based Method for GPS Localization Improvement in Unknown Semi-Obstructed Areas," *Sensors,* vol. 17, no. 1, p. 119, 2017, doi: 10.3390/s17010119.

[2] T. Suzuki and N. Kubo, "N-LOS GNSS signal detection using fish-eye camera for vehicle navigation in urban environments," *27th International Technical Meeting of the Satellite Division of the Institute of Navigation, ION GNSS 2014,* vol. 3, pp. 1897-1906, 2014.

[3] W. Wen, G. Zhang, and L. Hsu, "GNSS NLOS Exclusion Based on Dynamic Object Detection Using LiDAR Point Cloud," *IEEE Transactions on Intelligent Transportation Systems,* pp. 1-10, 2019, doi: 10.1109/TITS.2019.2961128.

[4] L.-T. Hsu, "Analysis and modeling GPS NLOS effect in highly urbanized area," *GPS Solutions,* vol. 22, no. 1, p. 7, 2018.

[5] W. Wen, G. Zhang, and L.-T. Hsu, "Correcting NLOS by 3D LiDAR and Building Height to improve GNSS Single Point Positioning," *NAVIGATION, Journal of the Institute of Navigation,* vol. 66, pp. 705– 718, 2019, doi: 10.1002/navi.335.

[6] I. Miller and M. Campbell, "Sensitivity Analysis of a Tightly-Coupled GPS/INS System for Autonomous Navigation," *IEEE Transactions on Aerospace and Electronic Systems,* vol. 48, no. 2, pp. 1115-1135, 2012, doi: 10.1109/TAES.2012.6178052.

[7] P. D. Groves and Z. Jiang, "Height Aiding, C/N0 Weighting and Consistency Checking for GNSS NLOS and Multipath Mitigation in Urban Areas," *Journal of Navigation,* vol. 66, no. 5, pp. 653-669, 2013, doi: 10.1017/S0373463313000350.

[8] P. D. Groves, "It's Time for 3D Mapping–Aided GNSS," *Inside GNSS Magazine,* 09/01 2016.

[9] M. Obst, S. Bauer, and G. Wanielik, "Urban multipath detection and mitigation with dynamic 3D maps for reliable land vehicle localization," in *Proceedings of the 2012 IEEE/ION Position, Location and Navigation Symposium*, 23-26 April 2012 2012, pp. 685-691, doi: 10.1109/PLANS.2012.6236944.

[10] L. Wang, P. D. Groves, and M. K. Ziebart, "GNSS Shadow Matching: Improving Urban Positioning Accuracy Using a 3D City Model with Optimized Visibility Scoring Scheme," *Navigation,* vol. 60, no. 3, pp. 195-207, 2013.

[11] P. D. Groves, "Shadow Matching: A New GNSS Positioning Technique for Urban Canyons," *Journal of Navigation,* vol. 64, no. 3, pp. 417-430, Jul 2011, doi: 10.1017/S0373463311000087.

[12] P. D. Groves, Q. Zhong, R. Faragher, and P. Esteves, "Combining Inertially-aided Extended Coherent Integration (Supercorrelation) with 3D-Mapping-Aided GNSS," *ION GNSS+ 2020,* 2020.

[13] L.-T. Hsu, Y. Hu, and S. Kamijo, "3D building model-based pedestrian positioning method using GPS/GLONASS/QZSS and its reliability calculation," *GPS Solutions,* vol. 20, no. 3, pp. 413-428, 2016.

[14] S. Miura, L.-T. Hsu, and F. Chen, "GPS Error Correction With Pseudorange Evaluation Using Three-Dimensional Maps," *IEEE Transactions on Intelligent Transportation Systems,* vol. 16, no. 6, pp. 3104-3115, 2015.

[15] N. Kbayer and M. Sahmoudi, "Performances Analysis of GNSS NLOS Bias Correction in Urban Environment Using a Three-Dimensional City Model and GNSS Simulator," *IEEE Transactions on Aerospace and Electronic Systems,* vol. 54, no. 4, pp. 1799-1814, 2018, doi: 10.1109/TAES.2018.2801658.

[16] H.-F. Ng, G. Zhang, and L.-T. Hsu, "A Computation Effective Range-based 3D Mapping Aided GNSS with NLOS Correction Method," *Journal of Navigation,* pp. 1-21, 2020.

[17] A. Kleusberg and P. J. G. Teunissen, *GPS for geodesy*, 2nd ed.. ed. Berlin; New York: Springer, 1998.

[18] R. B. Langley, "RTK GPS," *GPS World,* vol. 9, no. 9, pp. 70-76, 1998.

[19] P. J. G. Teunissen, "Least-Squares Estimation of the Integer GPS Ambiguities," *Invited lecture, section IV theory and methodology, IAG general meeting,* 1993.

[20] A. A. Verhagen, "The GNSS integer ambiguities: Estimation and validation," 2004.

[21] A. Leick, *GPS satellite surveying*. New York, N.Y.: Wiley (in English), 2004.

[22] N. Shaowei and C. Rizos, "Integrated method for instantaneous ambiguity resolution using new generation GPS receivers," in *Proceedings of Position, Location and Navigation Symposium - PLANS '96*, 22-25 April 1996 1996, pp. 254-261, doi: 10.1109/PLANS.1996.509086.

[23] M. Wei and K.-P. Schwarz, "Fast Ambiguity Resolution Using an Integer Nonlinear Programming Method," *Proceedings of the 8th International Technical Meeting of the Satellite Division of The Institute of Navigation (ION GPS 1995),* pp. 1101-1110, 1995.

[24] P. Teunissen, "On the computation of the best integer equivariant estimator," 2005.

[25] R. Odolinski and P. J. G. Teunissen, *On the Best Integer Equivariant Estimator for Low-cost Single-*

frequency Multi-GNSS RTK Positioning. 2020, pp. 499-508.

[26] T. Takasu and A. Yasuda, "Evaluation of RTK-GPS performance with low-cost singlefrequency GPS receivers," presented at the International Symposium on GPS/GNSS, Toyko, Japan, 2008.

[27] H. He, J. Li, Y. Yang, J. Xu, H. Guo, and A. Wang, "Performance assessment of single- and dual-frequency BeiDou/GPS single-epoch kinematic positioning," *GPS Solut,* vol. 18, no. 3, pp. 393-403, 2014, doi: 10.1007/s10291-013-0339-3.

[28] R. Odolinski, P. J. G. Teunissen, and D. Odijk, "First combined COMPASS/BeiDou-2 and GPS positioning results in Australia. Part I: single-receiver and relative code-only positioning," *Journal of Spatial Science,* vol. 59, no. 1, pp. 3-24, 2014, doi: 10.1080/14498596.2013.840865.

[29] R. Odolinski, P. J. G. Teunissen, and D. Odijk, "First combined COMPASS/BeiDou-2 and GPS positioning results in Australia. Part II: Single- and multiple-frequency single-baseline RTK positioning," *Journal of Spatial Science,* vol. 59, no. 1, pp. 25-46, 2014, doi: 10.1080/14498596.2013.866913.

[30] B. Li, Y. Feng, W. Gao, and Z. Li, "Real-time kinematic positioning over long baselines using triple-frequency BeiDou signals," *IEEE Transactions on Aerospace and Electronic Systems,* vol. 51, no. 4, pp. 3254-3269, 2015, doi: 10.1109/TAES.2015.140643.

[31] K. M. Pesyna, T. E. Humphreys, R. W. Heath, T. D. Novlan, and J. C. Zhang, "Exploiting Antenna Motion for Faster Initialization of Centimeter-Accurate GNSS Positioning With Low-Cost Antennas," *IEEE Transactions on Aerospace and Electronic Systems,* vol. 53, no. 4, pp. 1597-1613, 2017, doi: 10.1109/TAES.2017.2665221.

[32] R. S. Nerem and K. M. Larson, "Global Positioning System, Theory and Practice, 5th Edition," *Eos, Transactions American Geophysical Union,* vol. 82, no. 33, pp. 365-365, 2001, doi: 10.1029/01EO00224.

[33] T. Takasu and A. Yasuda, "Cycle Slip Detection and Fixing by MEMS-IMU/GPS Integration for Mobile Environment RTK-GPS," in *Proceedings of the 21st International Technical Meeting of the Satellite Division of The Institute of Navigation (ION GNSS 2008)*, Savannah, GA, 01/01 2008, pp. 64-71.

[34] H. Tokura and N. Kubo, *Effective Satellite Selection Methods for RTK-GNSS NLOS Exclusion in Dense Urban Environments*. 2016, pp. 304-312.

[35] H. Tokura and N. Kubo, "Efficient Satellite Selection Method for Instantaneous RTK-GNSS in Challenging Environments," *TRANSACTIONS OF THE JAPAN SOCIETY FOR AERONAUTICAL AND SPACE SCIENCES,* vol. 60, no. 4, pp. 221-229, 2017, doi: 10.2322/tjsass.60.221.

[36] P. J. G. Teunissen, R. Odolinski, and D. Odijk, "Instantaneous BeiDou+GPS RTK positioning with high cut-off elevation angles," *Journal of Geodesy,* vol. 88, no. 4, pp. 335-350, 2014/04/01 2014, doi: 10.1007/s00190-013-0686-4.

[37] R. Furukawa, N. Kubo, and A. El-Mowafy, "Prediction of RTK-GNSS Performance in Urban Environments Using a 3D model and Continuous LoS Method," in *Proceedings of the 2020 International Technical Meeting of The Institute of Navigation*, San Diego, California, 2020, pp. 763-771.

[38] R. Furukawa, N. Kubo, and A. El-Mowafy, "Verification of GNSS Multipath and Positioning in Urban Areas Using 3D maps," *IEICE Communications Express,* vol. advpub, 2020, doi: 10.1587/comex.2020XBL0096.

[39] F. Zimmermann, C. Eling, L. Klingbeil, and H. Kuhlmann, "Precise Positioning of Uavs - Dealing with Challenging Rtk-Gps Measurement Conditions during Automated Uav Flights," *ISPRS Annals of Photogrammetry, Remote Sensing and Spatial Information Sciences,* vol. 42W3, p. 95, August 01, 2017 2017, doi: 10.5194/isprs-annals-IV-2-W3-95-2017.

[40] G. Sohn and I. Dowman, "Data fusion of high-resolution satellite imagery and LiDAR data for automatic building extraction," *ISPRS Journal of Photogrammetry and Remote Sensing,* vol. 62, no. 1, pp. 43-63, 2007, doi: 10.1016/j.isprsjprs.2007.01.001.

[41] R. Wang, "3D building modeling using images and LiDAR: a review," *International Journal of Image and Data Fusion,* vol. 4, no. 4, pp. 273-292, 2013, doi: 10.1080/19479832.2013.811124.

[42] P. Jonge and C. C. J. M. Tiberius, "The LAMBDA method for integer ambiguity estimation: implementation aspects," *Delft Geodetic Computing Centre LGR Series,* vol. 12, 07/03 1998.

[43] E. Realini and M. Reguzzoni, "Gogps: open source software for enhancing the accuracy of low-cost receivers by single-frequency relative kinematic positioning," *Measurement Science and technology,* vol. 24, no. 11, p. 115010, 2013, doi: 10.1088/0957-0233/24/11/115010.

[44] P. J. G. Teunissen and C. Tiberius, "Integer least-squares estimation of the GPS phase ambiguities," 1994.

[45] P. Teunissen, "The invertible GPS ambiguity transformations," 1995.

[46] P. J. G. Teunissen, "On the GPS Double-Difference Ambiguities and their Partial Search Spaces," in *Geodetic Theory Today*, Berlin, Heidelberg, F. Sansò, Ed., 1995// 1995: Springer Berlin Heidelberg, pp. 39-48.

[47] d. J. Paul and C. Tiberius, "Integer Ambiguity Estimation with the Lambda Method," in *GPS Trends in Precise Terrestrial, Airborne, and Spaceborne Applications*, Berlin, Heidelberg, G. Beutler, W. G. Melbourne, G. W. Hein, and G. Seeber, Eds., 1996// 1996: Springer Berlin Heidelberg, pp. 280-284.

[48] R. Odolinski and P. J. G. Teunissen, "Best integer equivariant estimation: performance analysis using real data collected by low-cost, single- and dual-frequency, multi-GNSS receivers for short- to long-baseline RTK positioning," *Journal of Geodesy,* vol.

94, no. 9, p. 91, 2020/09/02 2020, doi: 10.1007/s00190-020-01423-2.

[49] G. Zhang, W. Wen, B. Xu, and L. Hsu, "Extending Shadow Matching to Tightly-Coupled GNSS/INS Integration System," *IEEE Transactions on Vehicular Technology,* vol. 69, no. 5, pp. 4979-4991, 2020, doi: 10.1109/TVT.2020.2981093.

[50] T. Pfeifer and P. Protzel, "Incrementally learned mixture models for gnss localization," 2019: IEEE, pp. 1131-1138.

[51] W. Wen *et al.*, "Urbanloco: a full sensor suite dataset for mapping and localization in urban scenes," *arXiv preprint arXiv:1912.09513,* 2019.

[52] E. Realini and M. Reguzzoni, "Gogps: open source software for enhancing the accuracy of low-cost receivers by single-frequency relative kinematic positioning," *goGPS: open source software for enhancing the accuracy of low-cost receivers by single-frequency relative kinematic positioning,* vol. 24, no. 11, p. 115010, 2013, doi: 10.1088/0957-0233/24/11/115010.

[53] P. J. G. Teunissen, "A canonical theory for short GPS baselines. Part IV: precision versus reliability," *Journal of Geodesy,* vol. 71, no. 9, pp. 513-525, 1997/08/01 1997, doi: 10.1007/s001900050119.

[54] D. Odijk and P. J. G. Teunissen, "ADOP in closed form for a hierarchy of multi-frequency single-baseline GNSS models," *Journal of Geodesy,* vol. 82, no. 8, p. 473, 2008/01/29 2008, doi: 10.1007/s00190-007-0197-2.

[55] R. Odolinski, P. J. G. Teunissen, and D. Odijk, "Combined BDS, Galileo, QZSS and GPS single-frequency RTK," *GPS Solutions,* vol. 19, no. 1, pp. 151-163, 2015/01/01 2015, doi: 10.1007/s10291-014-0376-6.

Hoi-Fung Ng received a Bachelor of Engineering (Honours) in Air Transport Engineering from The Hong Kong Polytechnic University, Hong Kong, in 2018.

He is currently an M.Sc. student at the Department of Mechanical Engineering, The Hong Kong Polytechnic University, Hong Kong. His research interests including GNSS localisation, navigation.

LI-TA HSU (S'09-M'15) received the B.S. and Ph.D. degrees in aeronautics and astronautics from National Cheng Kung University, Taiwan, in 2007 and 2013, respectively. He is currently an assistant professor with the Division of Aeronautical and Aviation Engineering, Hong Kong Polytechnic University, before he served as post-doctoral researcher in Institute of Industrial Science at University of Tokyo, Japan. In 2012, he was a visiting scholar in University College London, U.K. He is an Associate Fellow of RIN. His research interests include GNSS positioning in challenging environments and localisation for pedestrian, autonomous driving vehicle and unmanned aerial vehicle.